PCCP

Accepted Manuscript

ROYAL SOCIETY OF CHEMISTRY

www.rsc.org/pccp

Journal Name

RSCPublishing

ARTICLE

Pt nanoparticles supported on Sb-doped SnO_2 porous structures: developments and issues

Cite this: DOI: 10.1039/x0xx00000x

E. Fabbri,* A. Rabis, R. Kötz, and T. J. Schmidt

Received ooth January 2012,
Accepted ooth January 2012

DOI: 10.1039/x0xx00000x

www.rsc.org/

In this work, high surface area antimony doped tin oxide (Sb-SnO_2) has been synthesized by a modified sol gel synthesis method. The bulk and surface properties of the metal oxide support have been investigated as a function of the processing conditions. A change in the Sb-SnO_2 processing conditions, while preserving an overall invariant bulk composition, led to substantial modification of the surface stoichiometry. Accelerated stability test protocols have shown that the surface composition represents a crucial parameter for the electrochemical stability of Sb-SnO_2. Model Pt/Sb-SnO_2 electrodes have been developed depositing Pt nanoparticles by magnetron sputtering on the optimized Sb-SnO_2 porous surface. Significant enhancement in the corrosion stability upon 1000 potential cycling between 0.5 and 1.5 V (RHE) at 50 mV s^{-1} has been observed for the Pt/Sb-SnO_2 system compared to Pt/carbon.

Introduction

For a sustainable economic growth, many efforts have been directed in the last decades towards the development of efficient energy conversion systems using environmental friendly, renewable energy resources. In the scenario, particularly for automotive applications, the development of polymer electrolyte fuel cells (PEFCs) plays a critical role towards the development of a sustainable hydrogen-based-economy.[1] State-of-the-art PEFC cathodes are based on Pt nanoparticles supported on high surface area carbons. The latest developments in experimental techniques and computational studies have led to significant progress in the atomic level understanding of electrocatalyst behavior and to the development of advanced catalysts.[2] However, despite the good performance, Pt-based catalysts supported on high surface area carbons suffer from corrosion stability which represents at present one of the main issues hindering PEFC widespread market penetration.

Particularly for automotive applications, the cathode of a PEFC can experience under real operation conditions potentials as high as 1.5 V (RHE), which cause severe oxidation of the carbon support.[3] Carbon oxidation results in a decrease of the support surface area[4] with consequent detachment of the Pt nanoparticles and, thus, in a rapid failure of the fuel cell. Therefore, alternative support materials to carbons showing adequate stability under typical PEFC operative conditions are needed to meet the durability requirements for practical applications.[1] Besides being resistant against corrosion at high potentials, support materials for PEFCs must be also chemically stable under acidic conditions, good electronic conductors, and low cost and high surface area materials. In the search for alternative Pt supports, several materials such as graphitized carbons, carbides, and oxides, have been investigated so far.[5-7] Graphitized carbons show higher corrosion stability than high surface area carbon black;[8] however the use of carbon-based supports makes the corrosion issue only kinetically delayed and not thermodynamically resolved since carbon oxidation can occur at a potential as low as 0.207 V (RHE).[3] Other possible candidates as support materials are carbides, particularly WC due to its high electrical conductivity and chemical stability in acidic environment.[5-7] However, carbide-based supports will be again thermodynamically driven to oxidation and formation of the respective oxides under the high oxidative conditions of a fuel cell cathode, as already observed for WC.[9] Furthermore, since the synthesis of carbides is mainly through high temperature processes,[6] this class of materials cannot provide the required specific surface area for a support material. Therefore, the most successful approach in developing a high surface area, electron conductive, and corrosion resistant support appears to be the use of metal oxides. In fact, this class of materials can achieve high electrochemical stability when used in their highest oxidation state, high electronic conductivity through doping, as well as high surface area when produced by wet chemical synthesis methods, e.g., through flame pyrolysis.[10, 11]

Among chemical stable metal oxides in acidic conditions, we selected SnO_2-based supports because thermodynamic calculations[12] and experimental studies[13] have shown that SnO_2 in its highest oxidation state is redox inactive in the potential range of interest at pH=1. The first papers investigating the use of SnO_2 as support material for Pt catalysts appeared already in the late 70's.[14, 15] The main motivation for replacing carbon with SnO_2 was to take advantage of a strong-metal-support-interaction (SMSI). It was postulated that dispersing group VIII metals on transition metal oxides having surface cations able to be reduced to lower valence states would alter the metal catalytic and chemisorption properties.[16, 17] Indeed, it was consequently discovered that interactions between SnO_2 and Pt can occur, promoting the electrooxidation of CO and other low molecular weight alcohols, such as methanol and ethanol, on the Pt surface.[18-23] Furthermore, earlier studies on Pt nanoparticles supported on SnO_2 have shown excellent

corrosion stability compared to Pt supported on carbon upon potential cycling between 0.6 and 1.3 V (RHE) at room temperature[24] and between 0.7 and 1.2 V (RHE) at 70°C.[25] Besides the better corrosion resistance, Pt supported on SnO_2 or on a carbon/SnO_x mixture displayed higher catalytic activity towards oxygen reduction reaction (ORR) compared to Pt/carbon electrodes under the same experimental conditions.[26, 27] However, SnO_2 is an unfeasible support material due to its poor electronic conductivity. Therefore, doped SnO_2 supports must be developed in order to fulfil the conductivity requirement.[1]

Antimony-doped tin oxide is known to possess high electrical conductivity and it is a widely used material as a transparent conductive oxide, solid state gas sensor and catalyst for selective oxidation of hydrocarbons.[28] Sb-doped tin oxide has been already investigated as Pt support material alternative to carbons for improving corrosion resistance under typical PEFC cathode conditions. However contradictory results regarding the stability of Pt/Sb-doped SnO_2 systems were reported. Yin et al.[29] reported almost no change in the Pt electrochemical active surface area (ECSA) and in the mass activity towards ORR for Pt/Sb-doped SnO_2 system after 3000 potential cycles at 50 mV s^{-1} and between 0.35-0.85 V vs. SCE. Similarly, Kakinuma et al.[10] reported only a small decrease in ECSA for Pt/Sb-doped SnO_2 upon stepping the potential for 5000 times between 0.9 and 1.3 V (RHE), with a holding period of 30 s at each potential. Differently, Sasaki et al.[30] showed that significant degradation occurred upon 4000 potential cycles at 50 mV s^{-1} and between 0.6-1.3 V (RHE). Besides the use of different experimental conditions and stability test protocols, literature disagreements might result from a lack of support surface chemistry characterization. Thermal treatments at relatively high temperature are generally required to obtain crystalline metal oxides; however they can critically affect their structural properties, such as particle size and surface area, as well as their stoichiometry and dopant distribution. Particularly, severe thermal treatments can lead to a surface composition significantly different from that of the bulk. This phenomenon has been reported for Sb-doped SnO_2 oxides where dopant surface enrichment took place to an extent dependent upon bulk composition and calcination temperature or time.[31-37] It was also reported that the catalytic performance towards selective oxidation of hydrocarbons and CO for Sb-doped SnO_2 oxides strongly depends upon processing conditions, which also influence the Sb surface content.[33, 38] Therefore, it appears quite evident that a careful investigation of the surface properties of the metal oxide support is crucial for understanding its electrochemical properties and its stability under typical PEFC cathode conditions.

In this work, high surface area antimony doped tin oxide (Sb-SnO_2) has been synthesized by a modified sol gel synthesis method. Particular interest has been directed towards the investigation of the bulk and surface properties of the oxide support as a function of the processing conditions. Interestingly, it has been found that a change in the Sb-SnO_2 processing conditions, while preserving an overall invariant bulk composition, can lead to substantial modification of the surface stoichiometry. Accelerated stability test protocols have shown that the surface composition represents a crucial parameter for the electrochemical stability of antimony-doped tin oxide. After the evaluation of the Sb-SnO_2 electrochemical stability, 2D model electrodes have been developed by depositing Pt nanoparticles on the optimized Sb-SnO_2 porous surface. The electrochemical stability under typical PEFC cathode conditions, and the activity and selectivity towards ORR of the Pt/Sb-SnO_2 catalysts have been investigated by the thin-film rotating ring disk electrode (RRDE) technique.[39] Significant enhancement in the corrosion stability upon potential cycling between 0.5 and 1.5 V (RHE) has been observed for the Pt/ Sb-SnO_2 system compared to Pt/carbon under identical experimental conditions.

Experimental

Nominal $Sn_{0.95}Sb_{0.05}O_2$ (Sb-SnO_2) powder has been synthesized by a modified sol gel method. $SnCl_2$ (Aldrich, 99.99%) and Sb_2O_3 (Aldrich, 99.99%) has been used as staring materials. Both $SnCl_2$ and Sb_2O_3 were first dissolved in a 0.1 M HNO_3 aqueous solution. After the two solutions were mixed, NH_4OH solution (Aldrich) was used as a pH regulator (pH ~5). Chelation of the metal cations was then achieved by adding citric acid to the aqueous solution in a 2:1 ratio with respect to the total metal cations. Ethylene glycol was added in the last step to polymerize the organic precursor. The solution was heated under stirring and once the gel was obtained, it was washed and then dried at 150 °C overnight. Thermogravimetric analysis (TGA) of the powder precursor was performed in air, heating the sample at 5 °C min^{-1} from room temperature to 1000 °C (Perkin Elmer). The calcination process was carried out in O_2 at 550 °C for 2 and 10 h with a heating/cooling rate of 5 °C min^{-1}. After calcination, Sb-SnO_2 phase identification was carried out using X-ray diffraction (Bruker D8 system) with Cu Kα radiation (λ = 0.15418 nm) in Bragg-Brentano geometry. The specific surface area of the powder was determined by Brunauer-Emmett-Teller (BET). Sb-SnO_2 powder composition was investigated by energy-dispersive X-ray spectroscopy (EDX, Zeiss Supra) and by X-ray photoelectron spectroscopy (XPS). XPS measurements were performed using a VG ESCALAB 220iXL spectrometer (Thermo Fischer Scientific) equipped with an Al K_α monochromatic source (spot size: 500 μm, power: 150 Watt) and a magnetic lens system. Survey spectra were initially recorded at low resolution, and high resolution spectra were collected for quantitative analysis of Sb-SnO_2 composition. Microstructural analysis was carried out by scanning electron microscopy (SEM, Zeiss Supra) and transmission electron microscopy (TEM, FEI Morgagni 268).

Electrochemical impedance spectroscopy (EIS) was used to evaluate the electrical conductivity of the supports. The support powders were kept under a constant pressure of 0.6 MPa and the electrical resistivity was evaluated by EIS 4-wire measurements using metallic plate as current collectors. EIS measurements were performed at room temperature applying a 50 mV bias voltage, between 500 kHz and 0.1 Hz.

For the electro-chemical characterization, Sb-SnO_2 porous thin films were prepared by drop-coating an electrode ink on glassy carbon disks. The inks were prepared from a suspension made of 15 mg of the oxide powder, 20 μl of Nafion solution, and 5 ml of 2-propanol. Carbon inks were also prepared using the same composition by replacing the Sb-SnO_2 powder with acetylene black (AB, Alfa Aesar, surface area 85 m^2 g^{-1}). The working electrodes were immersed under potential control (0.7 V RHE) in 0.1 M $HClO_4$ electrolyte saturated with Ar at room temperature and the measurements were performed using a hydrogen reference electrode (RHE) and a gold counter electrode in a 3-electrode configuration. Cyclic voltammetry (CV) measurements were carried out to evaluate Sb-SnO_2 and AB electrochemical stability; 1000 potential cycles at room temperature, between 0.05 and 1.6 V (RHE), and with a scan rate of 50 mV s^{-1} were performed.

Pt/Sb-SnO_2 electrodes were prepared depositing Pt nanoparticles on the Sb-SnO_2 porous thin films by DC magnetron sputtering.[40] To test the electrochemical stability of Pt/Sb-SnO_2 catalysts under conditions similar to PEFC load-change and start/stop cycles,[41] CV measurements were performed over 1000 potential cycles between 0.5 and 1.5 V (RHE) using a scan rate of 50 mV s^{-1} at room temperature. The oxygen reduction reaction (ORR) activity and selectivity of the Pt/Sb-SnO_2 catalysts were measured before and after the stability test by rotating ring disk electrode (RRDE) technique. RRDE measurements were performed in O_2-saturated 0.1 M $HClO_4$ by cathodically scanning the disk electrode at 5 mVs^{-1} between 1 and 0.05 V (RHE) at different rotation speeds, while the Pt ring electrode was held at 1.2 V (RHE). The resulting disk polarization curves were corrected by the ohmic drop in the electrolyte measured by EIS. The collection efficiency of the Pt ring was 0.2 ± 0.02 determined according to ref. [42]. Stability tests and ORR activity measurements were also performed for Pt/AB electrodes prepared in the same way as described for the Pt/Sb-SnO_2 electrodes but replacing the Sb-SnO_2 with AB.

Results and discussion

Sb-SnO_2 supports: structural, chemical and electrical characterization

Several characterization techniques have been used to understand the physical properties of the antimony-doped tin oxide (Sb-SnO_2) support.

Thermogravimetric analysis (TGA) of the powder precursor is shown in Figure 1a. The main weight loss (~75 %) occurred between 130 and 550 °C due to the decomposition of the organic matrix. At higher temperatures no significant weight loss occurred. Based on the TGA result the calcination temperature for the Sb-SnO_2 powder precursor was set to 550 ˚C and the annealing process was carried out in oxygen atmosphere for 2 or 10 h. The O_2 atmosphere was selected in order to obtain metal oxides having cations in the highest oxidation state since this would represent the most thermodynamically stable system under the high oxidative conditions of a PEFC cathode.[1]

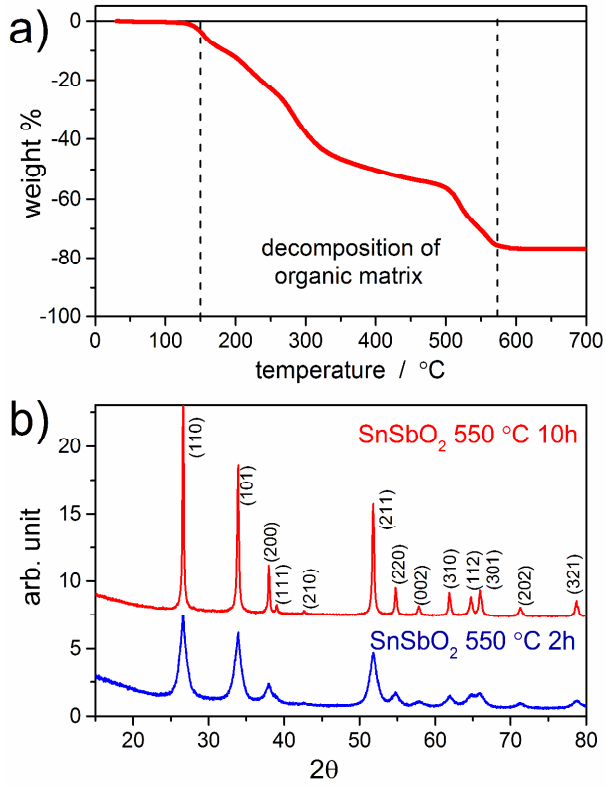

Fig. 1 TGA results of the Sb-SnO_2 powder precursor heated in air at 5 ˚C min^{-1} (a); XRD patterns of Sb-SnO_2 powder calcined at 500 ˚C for 2 h (blue line) or 10 h (red line) in O_2 (b).

Figure 1b shows the XRD patterns of Sb-SnO_2 powders after calcination at 550 ˚C for 2 and 10 h. Both calcination processes led to single phase materials with a rutile structure, even though the longer annealing time resulted in sharpening of the XRD peaks. The crystallite size, calculated by the Scherrer equation, increased from 6 ± 1 to 35 ± 2 nm increasing the calcination time from 2 to 10 h.

The specific surface area of Sb-SnO_2 powders was measured by Brunauer-Emmett-Teller (BET) analysis; for the powder calcined at 500 ˚C for 2 h the BET surface area was 53 ± 8 m^2 g^{-1}, while for the sample calcined for 10 h a significant decrease in BET surface area was observed (18 ± 5 m^2 g^{-1}). Scanning electron microscope (SEM) analysis revealed that increasing the annealing time not only increased the average particle size but also the amount and the size of particle agglomerates.

For the highest surface area Sb-SnO_2 powder transmission electron microscopy (TEM) investigations were carried out to unveil the primary particle size. A typical TEM image is shown in Figure 2; primary particle size is in the range of 10-20 nm, with the primary particles forming larger agglomerates.

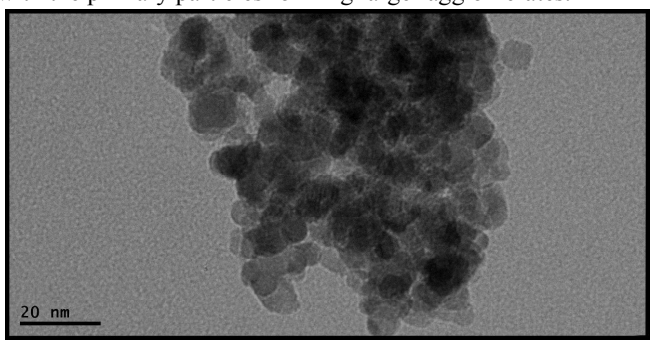

Fig. 2 Typical TEM image of Sb-SnO_2 powder after calcination at 550 ˚C for 2 h.

Besides structural and microstructural characterizations, the chemical composition of the calcined powders was investigated by means of energy-dispersive X-ray spectroscopy (EDX) and X-ray photoelectron spectroscopy (XPS). Both techniques allow the evaluation of the chemical composition, but while for the EDX the penetration depth of the X-ray probe is typically in the micrometer range, for the XPS the penetration depth is generally within the first nanometers. Therefore, with an average primary particle size in the 10-20 nm range, we can assume that by using both techniques we can distinguish between the bulk and the near-surface chemical composition. EDX and XPS results are summarized in Table 1. EDX showed that independently of the annealing process the two samples presented very close values of bulk Sb content, which resulted slightly higher than the projected value (5 at%). However, as reported in ref. [29] doping SnO_2 with 5 or 8 at% Sb only results in a relative small difference in electrical conductivity. Contrarily to the EDX results, XPS analysis showed different Sb content as a function of the calcination time. Comparing the EDX and XPS results (bulk vs. surface composition,

Table I Sb at% measured by EDX and XPS for Sb-SnO_2 powders as calcined at 550 °C for 2 and 10 h, and after the electrochemical stability test in 0.1 M $HClO_4$ at 50 mVs^{-1} between 0.05 and 1.6 V RHE.

Sb-SnO_2 annealed at 550°C for		XPS Sb at%	EDX Sb at%
2 h	As calcined	6.7± 0.5	8.5 ± 0.5
	After stability test	8.9 ± 1.0	8.4 ± 0.95
10 h	As calcined	14.6 ± 0.8	8.3 ± 0.6
	After stability test	5.6 ± 1.1	0.8 ± 0.6

respectively) it is evident that the 10 h annealing process led to segregation of Sb ions at the surface. Formation of a surface rich in the dopant element after a high temperature or prolonged annealing treatment was already observed for different SnO_2 dopant elements such as Y, Ce, In, Nb and Sb.[31-37, 43] Cross and Pyke[35] investigated the effect of calcination treatment on the surface composition of Sb-doped SnO_2 oxides prepared by a co-precipitation method. Via XPS analysis antimony surface concentration was measured varying the calcination temperature (at a constant calcination period of 16 h); an increase in Sb surface concentration was observed for temperature above ~400 ˚C, reaching a maximum at 1000 ˚C. At higher temperatures, a decrease in Sb concentration was observed due to the formation of macroscopically distinguishable Sb_2O_4 phase and consequent vaporization of the latter oxide. The authors concluded that the oxide preparation forces Sb into a non-favorable environment, so that at high temperatures surface segregation takes place allowing an energetically more favorable state for antimony ions.[35] Similarly, Dusastre et al.[33] showed that a variation of the calcination temperature produced systematic changes in surface composition of Sb-doped tin oxide as determined by XPS analysis. Furthermore it was observed that at constant calcination temperature and time the Sb surface enrichment is strongly influenced by the bulk composition (by a factor of 10 between 0.5 and 5 at% Sb-doped compounds at 800 °C).[33] It has been also reported that at low doping levels (below ~ 10%) antimony is mostly present with a 5+ oxidation state. With a further increase in the doping concentration, antimony ions appear also in 3+ oxidation state, with the Sb(III) content even exceeding the Sb(V) one for high doping level.[37, 44] The latter situation results in a decrease of the electrical conductivity since when both Sb(V) and Sb(III) exist, compensating effects take place. [44] In fact, Sb(V) acts as electron donor, forming a shallow donor level close to SnO_2 conduction band, while Sb(III) behaves as an electron acceptor. Computational studies of Slater et al.[45] suggested that Sb(III) is mostly associated with in-plane surface oxygen species, while Sb(V) is incorporated below bridging oxygen ions in a more bulk-like environment. Therefore, when surface dopant segregation occurs due to harsh processing conditions, the Sb ions occupying the upmost surface layers are expected to be mostly present as Sb(III) ions, which would not act as n-type donors but instead trap electron pairs reducing the oxide conductivity.[46]

Electrochemical impedance spectroscopy (EIS) has been used to evaluate the electrical conductivity of the Sb-SnO_2 supports as a function of the calcination temperature, i.e. dopant distribution. The Sb-SnO_2 powders were kept under a constant pressure of 0.6 MPa and the electrical resistivity was evaluated by EIS 4-wire measurements at room temperature. It must be remarked that the present conductivity measurements can only give relative conductivity results, i.e. applying a higher pressure would result in a lower oxide resistivity due to an improved contact between particles and agglomerates. Figure 3 shows typical EIS complex impedance plane plots obtained for the Sb-SnO_2 samples calcined at 550˚C for 2 and 10 h. Both the Nyquist plots in Figure 3 show in the low frequency range two small depressed semicircles most probably related to the oxide/current collector contact resistance. At high frequency, for the sample calcined for 2 h a resistance in series with an inductive contribution (the latter originating from the measuring device and the electrical connections) were observed. For the sample calcined for 10 h a high frequency semicircle, originating from the oxide impedance, appeared. The difference in the two Nyquist plots arises from the different oxide impedances (note the different x-axis scale); assuming the same specific capacitance for the two samples, the lower the material impedance the higher the frequencies at which the material response occurs.[47] Therefore, for the sample calcined for 2 h and showing lower impedance, the semicircle corresponding to the oxide impedance is observed at too high frequencies, which cannot be measured due to frequency limits of the EIS spectrometer. The overall support powder resistance was determined from the first intercept at high frequency of the Nyquist plot with the real axis. Knowing the compressed powder thickness and the geometric electrode area, the resistivity was evaluated to be 50 ± 10 Ω cm and 2700 ± 60 Ω cm for the sample calcined at 550 ˚C for 2 and 10 h, respectively. The increase in resistivity of more than one order of magnitude for the sample annealed at 550 ˚C for 10 h can result from (i) inhomogeneous distribution of the Sb ions, (ii) compensating effects between Sb(III) and Sb(IV) ions, (iii) higher contact resistance between particles and agglomerates, or (iv) from combination of all factors. For comparison, the resistivity of acetylene black was also measured in the same conditions and a value of 0.87 ± 0.04 Ω cm was obtained in agreement with literature data.[48]

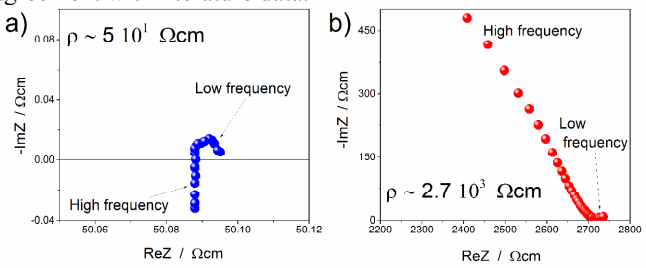

Fig. 3 Typical Nyquist plots for Sb-SnO_2 powders calcined at 550 ˚C for 2 h (a) and for 10 h (b) recorded at room temperature and under a constant pressure of 0.6 MPa.

Sb-SnO_2 supports: electrochemical characterization

The dopant distribution might also influence the electrochemical behavior of Sb-SnO_2 in aqueous environment. It was already reported in heterogeneous catalysis that Sb surface segregation affected the rate of surface-catalyzed combustion of hydrocarbons and carbon monoxide over Sb-doped SnO_2 oxides.[33, 38] In the present work, electrochemical stability test of Sb-SnO_2 powder supports were carried out by cyclic voltammetry (CV) measurements in Ar-saturated 0.1 M $HClO_4$ at room temperature. Thin porous films of Sb-SnO_2 powders calcined at 550 ˚C for 2 and 10 h were potential cycled at 50 mV s^{-1} between 0.05 and 1.6 V for 1000 times. By the use of this electrochemical stability test it is possible to simulate accelerated PEFC load-change and start/stop cycles, and also to test the stability of the oxide in more reductive

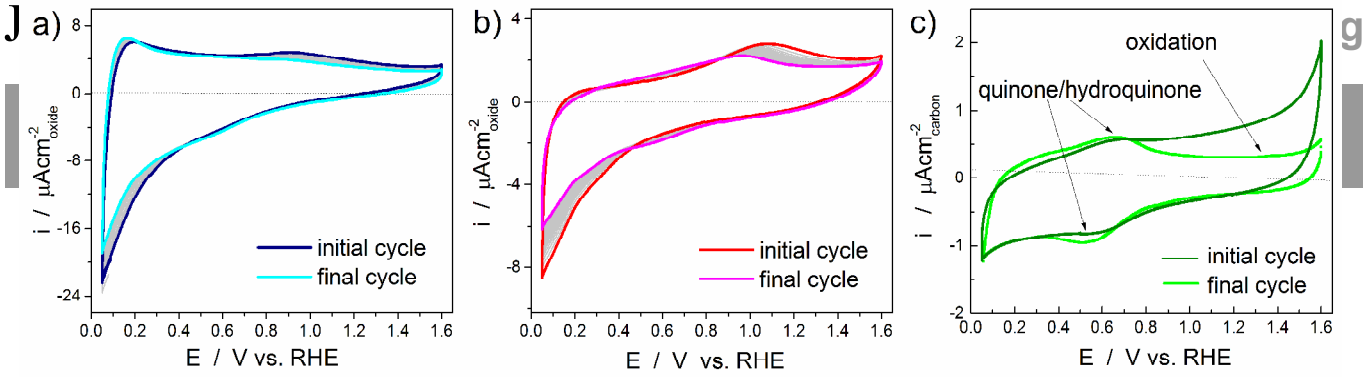

Fig. 4 Cyclic voltammograms of Sb-SnO_2 calcined at 550 ˚C for 2 h (a) and 10 h (b), and of acetylene black carbon (c) at 50 mVs^{-1} in Ar-saturated 0.1 M $HClO_4$ initial (3th cycle) and final (1000th cycle) potential scan between 0.05 and 1.6 V RHE at 50 mVs^{-1} and room temperature. The current is normalized by the surface area of the support as measured by BET.

conditions (between 0.05 and 0.5 V RHE) than the typical operating PEFC potentials. For comparison, the same stability test was also performed using acetylene black carbon (Alfa Aesar), which was selected for a reason that will become clear later. Figure 4 shows the CVs related to the 3th and the 1000th cycles for the Sb-SnO_2 calcined at 550 ˚C for 2 h (a) and for 10 h (b), and for the acetylene black carbon (c). For the Sb-SnO_2 calcined at 550 ˚C for 2 h a fairly visible redox couple at about 0.9-0.6 V (RHE) could be observed. The redox couple can be associated to reduction /oxidation of Sb ions between 5+ and 3+ oxidation state according to:[49]

$$Sb_2O_5 + 4H^+ + 4\,e^- \rightleftharpoons Sb_2O_3 + 2H_2O \qquad E^\circ = 0.649 \text{ V vs. NHE}$$

For the Sb-SnO_2 sample calcined at 550 ˚C for 10 h, the redox couple was more clearly visible, consistently with the larger surface concentration of Sb ions for this sample. Furthermore, the larger potential difference between the redox peaks could account for the initial lower conductivity of the sample calcined at 550 ˚C for 10 h (see Fig. 3). After the stability test for the Sb-SnO_2 calcined at 550 ˚C for 2 h a decrease of 7% and 4.5% for the anodic and cathodic charge, respectively, was observed. For the sample calcined for 10 h a strong modification of the CV was observed, going towards a reduction of ~12% of both anodic and cathodic charges. Even though it is not possible to give a quantitative evaluation of the support degradation during the electrochemical stability test by merely CV measurements, the strong change in the voltammogram for the sample annealed at 550 ˚C for 10 h suggests that a significant modification of this Sb-SnO_2 support occurred. Therefore, the present results indicate that the doping distribution in Sb-SnO_2 is also a crucial factor in determining the electrochemical stability upon potential cycling in aqueous environment.

Figure 4c illustrates the CVs of acetylene black carbon before and after the same electrochemical stability test. As expected, a strong oxidation current at the highest potential was observed, mostly due to oxidation of the carbon support. Upon cycling the anodic current strongly decrease and growth of the quinone/hydroquinone redox couple around 0.55-0.7 V (RHE) was observed. Therefore, the comparison of the cyclic voltammograms before and after the electrochemical stability test indicates that the better corrosion resistant support is the metal oxide Sb-SnO_2 having homogeneous distribution of the dopant.

For a quantitative evaluation of the support corrosion during the potential cycling, XPS and EDX analysis was carried out for the two oxide supports also after the stability test. Table 1 reports the bulk (measured by EDX) and surface (measured by XPS) composition for the Sb-SnO_2 samples after the electrochemical stability test. For the sample annealed at 550 ˚C for 2 h a slight enrichment of Sb concentration occurred (from 6.7 to 8.9 at%), while almost no change in the bulk concentration could be observed. Differently, for the Sb-SnO_2 annealed at 550 ˚C for 10 h and already presenting Sb enrichment at the surface, a decrease in the surface antimony content took place. Also the Sb bulk concentration significantly decreased, indicating that a loss of Sb occurred upon potential cycling. Therefore, it appears that when the surface layers already present dopant enrichment potential cycling between 0.05 and 1.6 V (RHE) favours a further migration of Sb at the surface followed by Sb dissolution in the electrolyte, leaving the bulk composition depleted in dopant concentration. Differently, starting from a Sb-SnO_2 support with homogeneous Sb distribution, potential cycling only results in a minor Sb segregation at the surface without further dissolution of the dopant.

Combining literature data about surface Sb segregation[31-37] and the present results it is possible to develop a general segregation/dissolution mechanism, schematically shown in Figure 5. Starting from a situation where Sb ions are homogeneously distributed into the SnO_2 matrix, either calcination temperature, calcination time, and potential cycling can induce an initial Sb surface enrichment. Sb surface segregation can further proceed till Sb-oxide is formed on the SnO_2 surface and, then, finally removed (vaporized in case of harsh annealing process or dissolved in case of potential cycling in aqueous media), leaving a bulk material poor in dopant concentration.

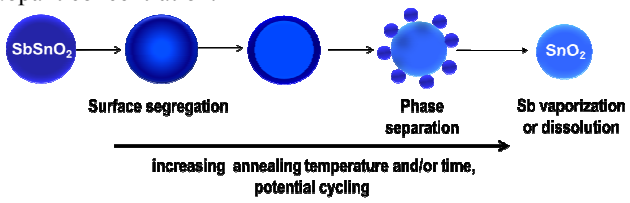

Fig. 5 Schematic sketch representing segregation/dissolution process of Sb dopant in SnO_2 matrix upon harsh annealing treatment and/or potential cycling in aqueous environment.

Therefore the present results indicate that not only in heterogeneous catalysis Sb surface segregation can lead to different catalytic properties.[33, 38] Also in terms of electrochemical stability achieving a homogeneous Sb distribution within the SnO_2 host matrix is essential to maximize the corrosion stability of Sb-doped SnO_2 in acidic media. Having established the superior electrochemical stability of the Sb-SnO_2 support calcined at 550 ˚C for 2 h, more detailed electrochemical investigations have been carried out on this support material. Particularly, CV measurements were performed progressively opening the potential window within 0 and 1.4 V (RHE) and also by extending the potential range down to -0.4 V (RHE). Figure 6a shows the cyclic voltammograms of Sb-SnO_2 calcined at 550 ˚C for 2 h with a lower potential limit of 0 V (RHE) and progressively increasing the upper potential from 0.8 to 1.4 V (RHE). The CV measurements in Figure 6a showed that the more positive the upper potential limit during anodic sweep the larger the reduction current in the subsequent cathodic sweep becomes. Table 2 reports the anodic and cathodic charges varying the potential window. When the upper potential limit is above 1 V (RHE), the cathodic charges exceeded the positive ones by about 5%, while in the 0-0.8 V RHE potential range the cathodic charges were ~10% higher than the anodic ones. This result suggests that a non-reversible process is occurring at the surface of Sb-SnO_2 metal oxide. The electrochemical properties of Sb-SnO_2 were further investigated in the negative potential range. Figure 6b shows a CV measurement between 1 and -0.4 V (RHE). A further reduction current was observed going to more cathodic potential than 0 V (RHE), which is most likely associated to reduction of Sb-SnO_2. By the use of a Pt ring electrode held at a constant potential of 0.4 V (RHE), where H_2 oxidation is purely under mass transport limited control, it was possible to exclude that H_2 evolution occurred from the Sb-SnO_2 surface. After -0.4 V (RHE) being reached, on the subsequent anodic sweep a peak at about 0.35-0.4 V (RHE) appeared; the latter was already observed for SnO_2 samples[13] and mostly associated to SnO_2 re-oxidation. Therefore, it appears that potentials more negative than 0 V (RHE) can rapidly reduce the Sb-SnO_2 surface.

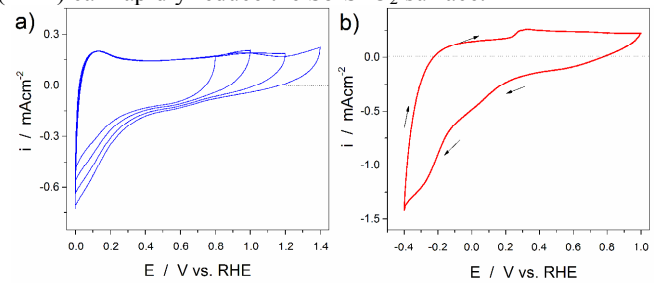

Fig. 6 CV measurements for Sb-SnO_2 calcined at 550 ˚C for 2 h in 0.1 M $HClO^4$ at 50 mVs^{-1} and room temperature varying the potential window (RHE).

Table II Anodic and cathode charge ($\mu C\ cm^{-2}{}_{oxide}$) calculated in different potential ranges (RHE) from the cyclic voltammograms shown in Figure 6a.

Charge ($\mu Ccm^{-2}{}_{oxide}$)	0-0.8 V	0-1.0 V	0-1.2 V	0-1.4 V
anodic	30.0	38.8	47.1	55.6
cathodic	33.2	40.8	49.6	58.6

Pt nanoparticles supported on Sb-SnO_2: electrochemical activity, selectivity, and stability

The Pt/Sb-SnO_2 catalysts were prepared by depositing on the top layer of Sb-SnO_2 porous thin film 10 μg cm^{-2} of Pt by magnetron sputtering. In a previous work[50] the Pt deposition parameters were optimized to obtain the desired Pt loading and the primary particle size was determined to be 2-3 nm in diameter; however particle agglomerates are expected to be created on the surface of Sb-SnO_2. The catalytic activity towards the ORR for the Pt/Sb-SnO_2 catalysts was investigated by rotating ring disk electrode (RRDE) measurements. Figure 7 shows the ORR polarization curves on a negative-going potential scan for Pt/Sb-SnO_2 catalyst in O_2-saturated 0.1 M $HClO_4$, at 5 mV s^{-1} and for different rotation speeds. For each ORR curve, a typical mass transport/kinetically mixed region at low overpotential and a mass transport limited region at higher overpotential was observed, comparable to those obtained for conventional Pt/carbon catalysts.[42, 51, 52] At potentials more cathodic than ~0.1 V (RHE), a decrease in the ORR current can be observed. Similar behaviour has been observed for Pt polycrystalline[52] and single crystal electrodes.[53] Literature studies[53] ascribe such decrease in ORR current to an increase in the hydrogen underpotential deposition (H_{upd}) coverage which results to a larger amount of hydrogen peroxide produced during the ORR. Indeed, as shown in Figure 7, the corresponding ring current (due to the oxidation of the hydrogen peroxide produced on the disk) confirmed an increase in H_2O_2 formation at high overpotentials. At the lowest measured potential (50 mV RHE) the H_2O_2 production reach up to 13 %, while it progressively decreased to 7% at 0.1 V (RHE) and went to almost zero at potential higher that ~0.6 V (RHE), similar to relatively low Pt loading catalysts.[13, 52] The small amount of hydrogen peroxide formation indicates that the ORR on Pt supported on Sb-SnO_2 mostly invlolves a 4-electrons transfer process. From the Levich-Koutecky relationship, a first order dependence of ORR kinetics and a 4 electron transfer process could be confirmed for the Pt/Sb-SnO_2 catalysts.

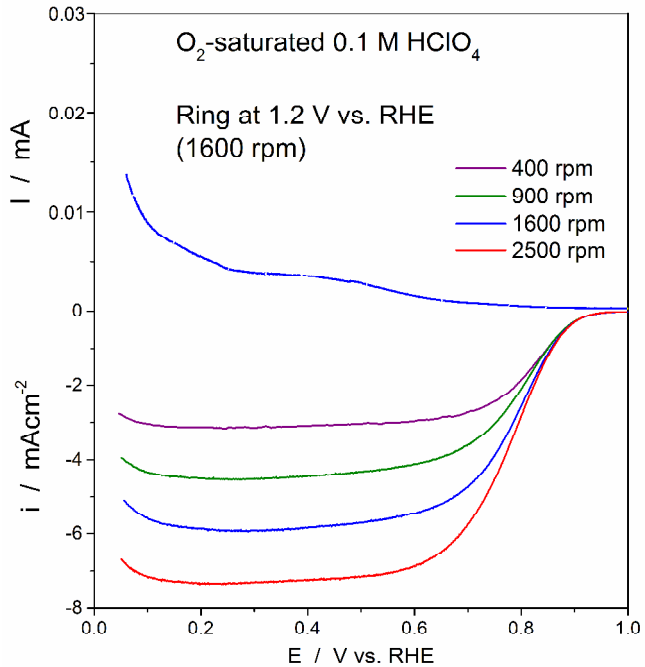

Fig. 7 Ring and disc current/potential curves for 10 μgcm^{-2} Pt on Sb-SnO_2 in O_2-saturated 0.1 M $HClO_4$, at room temperature,

5 mVs^{-1} and cathodic direction of the potential scan; the Pt ring electrode was held at 1.2 V (RHE).

After having established that the ORR on Pt nanoparticles supported on Sb-SnO_2 follows a 4 electron transfer process, the electrochemical stability of the catalysts has been investigated by performing 1000 potential cycles between 0.5 and 1.5 V (RHE) at 50 mV s^{-1} and in Ar-saturated 0.1 M $HClO_4$. The present stability test is helpful to mimic the PEFC load-change cycles and the potential excursion at the cathode during start/stop cycles.[41] Figure 8 shows the initial and final CV measurements of the stability test for the Pt/Sb-SnO_2 catalyst.

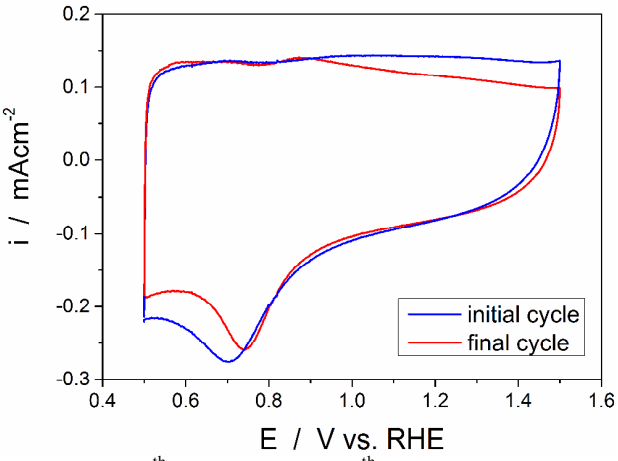

Fig. 8 initial (5th) and final (1000th) cycle of the Sb-SnO_2 electrochemical stability test performed by CV at 50 mVs^{-1} between 0.5 and 1.5 V (RHE) in Ar-saturated 0.1 M $HClO_4$.

The most noticeable change in the cyclic voltammograms upon cycling is related to the shift of the Pt-oxide reduction peak (~0.7 V RHE) towards higher potential. The shift in the Pt-oxide reduction peak can be correlated to Pt nanoparticle growth and agglomeration during potential cycling. During potential cycling in the 0.5-1.5 V (RHE) range, Pt undergoes to different degradation processes, namely dissolution, Ostwald-ripening, and coalescence.[3, 8, 54] The latter phenomena lead to growth and agglomeration of the Pt nanoparticles. It has been previously reported that the Pt-oxide reduction peak potential can vary with Pt particle size and distribution.[51, 52, 55-60] Particularly, isolated nanoparticles show higher adsorption energy of oxygenated species compared to extended surfaces.[52, 61] Therefore, the Pt-oxide reduction peak occurs at more cathodic potential for isolated nanoparticles compared to agglomerates/extended layers.[52] In the present work, the shift to higher potentials of the Pt-oxide reduction peak during the potential cycling indicates a growth/agglomeration of the Pt nanoparticles.

To understand the change in Pt activity before and after the electrochemical stability test, the ORR activity has been measured before and after the potential cycling. Figure 9 shows ohmic and mass transport corrected polarization curves in O_2-saturated 0.1 M $HClO_4$ measured on a negative-going sweep at 5 mV s^{-1} and 1600 rpm for pristine Pt/Sb-SnO_2 catalysts and after 1000 potential cycling between 0.5 and 1.5 V (RHE). The activity of the pristine Pt/Sb-SnO_2 catalyst (taken as the ORR kinetic current density at 0.9 V RHE) was 0.155 ± 0.022 mA cm^{-2}. Normalizing the ORR kinetic current by the Pt loading a mass activity of 15.5 ± 2.2 mA mg_{Pt}^{-1} was obtained. After the stability test the ORR activity for the Pt/Sb-SnO_2 catalyst decreased by 26 ± 10%. It must be highlighted that replacing carbon with a more electrochemically stable support material, only the support corrosion is suppressed but not the Pt dissolution, Ostwald-ripening, and coalescence. Therefore, decrease of the Pt/support catalytic activity upon potential cycling within 0.5-1.5 V (RHE) range is expected due to the above mentioned Pt degradation phenomena. In order to compare the stability of the Pt/Sb-SnO_2 catalyst with that of a Pt/carbon system we selected as carbon support commercial acetylene black (AB). AB shows similar surface area than Sb-SnO_2 and, therefore, magnetron sputtering of Pt nanoparticles would lead to similar Pt distribution on the two supports. Figure 9 shows ohmic drop and mass transport corrected ORR curves taken on a negative going scan at 5 mV s^{-1} and 1600 rpm before and after the stability test. The ORR kinetic current at 0.9 V (RHE) for the Pt/AB pristine catalysts was 0.125 ± 0.019 $mAcm^{-2}$, which corresponds to a mass activity of 12.5 ± 1.9 $mAmg_{Pt}^{-1}$. After the electrochemical stability test, the ORR activity of the Pt/AB catalysts decrease by 65 ± 7 %, basically more than a factor of 2 compared to Pt/Sb-SnO_2 after the same stability test. These results demonstrate a superior corrosion resistance upon potential cycling of the Pt/Sb-SnO_2 compared to Pt/AB.

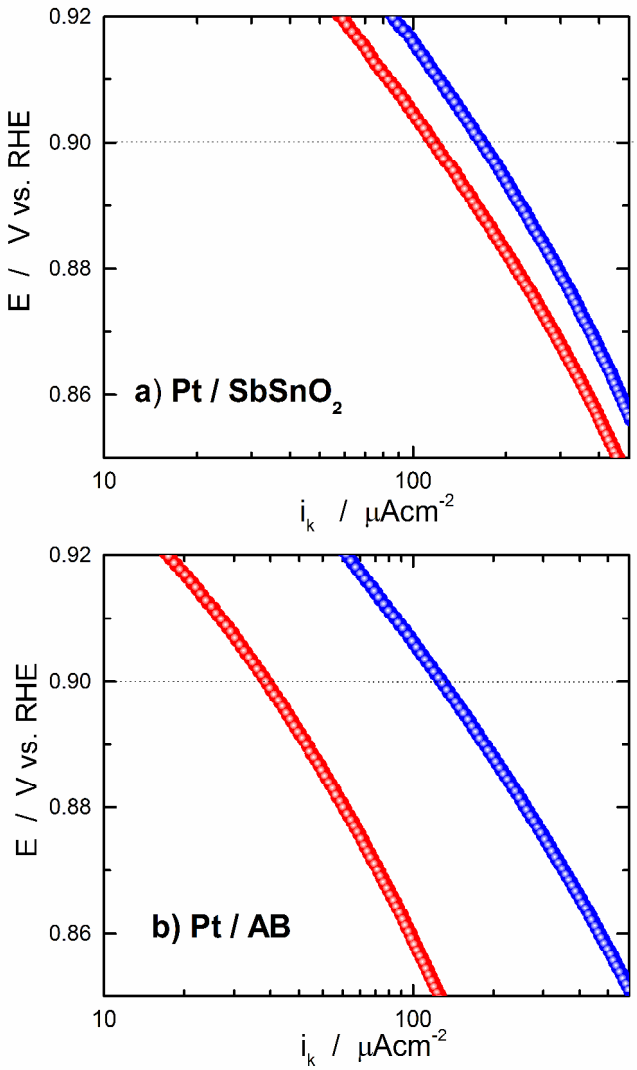

Fig. 9 Tafel plots of Pt/Sb-SnO_2 (a) and Pt/AB (b) catalysts before (blue symbols) and after (red symbols) stability test. The polarization curves are measured on a negative-going sweep at

5 mVs^{-1} and 1600 rpm in O_2-saturated 0.1 M $HClO_4$. The polarization curves are ohmic-drop and mass transport corrected.

The minor degradation in terms of ORR activity of the Pt/Sb-SnO_2 catalyst could simply derive from the better electrochemical stability of Sb-SnO_2 metal oxide compared to carbon. During potential cycling, carbon oxidation leads to detachment of the Pt nanoparticles with consequent dissolution or agglomeration of the latter. Preventing the degradation of the support through the use a stable metal oxide slows avoiding Pt loss due to the support failure. Furthermore, based on literature data, a SMSI between oxide support and Pt might take place. The occurrence of a SMSI between Pt and Sb-doped SnO_2[29] or between Pt and TiO_2 and WO_3[62] was already reported based on XPS data analysis. Further measurements are under progress in order to understand if a SMSI occurs also for the present catalyst systems.

Conclusions and outlooks

The present results have demonstrated that the careful analysis of the metal oxide surface composition is of high importance for the development of stable and conductive support materials. In case of Sb-SnO_2, a prolonged annealing treatment results in surface layers, enriched in Sb ions, which are involved in electrochemical reactions. This leads to a reduced electrical conductivity and electrochemical corrosion resistance. Based on the present results, the controversial results reported in the literature about the stability of Pt supported on Sb-doped tin oxides may be explained by a difference in the support surface chemistry. Therefore, it appears misleading pointing to Sb-doped SnO_2 as a corrosion resistant or unstable PEFC support material; the nominal bulk composition and the processing conditions seem to play a critical role in determining the corrosion resistance of Sb-SnO_2 upon potential cycling in acidic environment. Sb ions tend to segregate to SnO_2 surface upon harsh annealing treatments or potential cycling, leading eventually to Sb vaporization or dissolution, respectively. However, minimizing the concentration of Sb ions at the surface, still keeping a reasonable electrical conductivity, may kinetically delay this phenomenon leading to a much more stable Pt support than commercial carbon. Upon potential cycling in 0.1 M $HClO_4$ between 0.05 and 1.6 V (RHE) at 50 mV s^{-1}, the optimized Sb-SnO_2 support have shown improved corrosion resistance compared to carbon. This result has been further confirmed by the superior stability of Pt/Sb-SnO_2 catalysts compared to Pt/carbon catalysts after the stability test. Preventing the support corrosion has allowed avoiding loss of Pt during the accelerated corrosion stability test, which can account for the superior stability of the Pt/Sb-SnO_2 catalyst compared to the Pt/carbon one.

Acknowledgements

This work was supported by CCEM Switzerland and Umicore AG & Co KG within the project DuraCat. We gratefully thank Michael Horisberger for the sputtering of the Pt catalyst onto the Sb-SnO_2 support.

Notes and references

[a] Electrochemistry Laboratory, Paul Scherrer Institut, 5232 Villigen PSI, Switzerland.

*E. Fabbri: emiliana.fabbri@psi.ch

1. A. Rabis, P. Rodriguez and T. J. Schmidt, *Acs Catal*, 2012, **2**, 864-890.
2. E. Fabbri and T. J. Schmidt, *Platinum-Based Cathode Catalysts for Polymer Electrolyte Fuel Cells in Encyclopedia of Applied Electrochemistry, Springer Science + Business Media LLC, New York, R.F. Savinell, K. Ota, G, Krysa (Eds.),*, 2013, DOI: 10.1007/SpringerReference_303646
3. F. N. Büchi, M. Inaba and T. J. Schmidt, *Polymer Electrolyte Fuel Cell Durability; Eds.; Springer Science and Business Media LLC: New York* 2009, 199-221.
4. H. Schulenburg, B. Schwanitz, N. Linse, G. G. Scherer, A. Wokaun, J. Krbanjevic, R. Grothausmann and I. Manke, *J Phys Chem C*, 2011, **115**, 14236-14243.
5. E. Antolini and E. R. Gonzalez, *Solid State Ionics*, 2009, **180**, 746-763.
6. Y. Y. Shao, J. Liu, Y. Wang and Y. H. Lin, *J Mater Chem*, 2009, **19**, 46-59.
7. S. Sharma and B. G. Pollet, *J Power Sources*, 2012, **208**, 96-119.
8. K. Hartl, M. Hanzlik and M. Arenz, *Energ Environ Sci*, 2011, **4**, 234-238.
9. H. Chhina, S. Campbell and O. Kesler, *J Power Sources*, 2007, **164**, 431-440.
10. K. Kakinuma, M. Uchida, T. Kamino, H. Uchida and M. Watanabe, *Electrochim Acta*, 2011, **56**, 2881-2887.
11. K. Kakinuma, Y. Chino, Y. Senoo, M. Uchida, T. Kamino, H. Uchida, S. Deki and M. Watanabe, *Electrochim Acta*, 2013, **316–324**, 316– 324.
12. M. Pourbaix, *Atlas of Electrochemical Equilibria*, Cebelcor, 1974.
13. A. Rabis, D. Kramer, E. Fabbri, M. Worsdale, R. Kötz and T. J. Schmidt, *submitted to J. Phys. Chem. C*, 2014.
14. V. B. Hughes and B. D. McNicol, *J Chem Soc Farad T 1*, 1979, **75**, 2165-&.
15. M. Watanabe, S. Venkatesan and H. A. Laitinen, *J Electrochem Soc*, 1983, **130**, 59-64.
16. S. J. Tauster and S. C. Fung, *J Catal*, 1978, **55**, 29-35.
17. S. J. Tauster, S. C. Fung, R. T. K. Baker and J. A. Horsley, *Abstr Pap Am Chem S*, 1981, **181**, 50-Coll.
18. J. Y. Xu, D. Aili, Q. F. Li, C. Pan, E. Christensen, J. O. Jensen, W. Zhang, G. Y. Liu, X. D. Wang and N. J. Bjerrum, *Journal of Materials Chemistry A*, 2013, **1**, 9737-9745.
19. S. Axnanda, W. P. Zhou and M. G. White, *Phys Chem Chem Phys*, 2012, **14**, 10207-10214.
20. K. S. Lee, I. S. Park, Y. H. Cho, D. S. Jung, N. Jung, H. Y. Park and Y. E. Sung, *J Catal*, 2008, **258**, 143-152.
21. A. O. Neto, M. Brandalise, R. R. Dias, J. M. S. Ayoub, A. C. Silva, J. C. Penteado, M. Linardi and E. V. Spinace, *Int J Hydrogen Energ*, 2010, **35**, 9177-9181.
22. L. Jiang, L. Colmenares, Z. Jusys, G. Q. Sun and R. J. Behm, *Electrochim Acta*, 2007, **53**, 377-389.
23. Y. G. Chen, J. J. Wang, X. B. Meng, Y. Zhong, R. Y. Li, X. L. Sun, S. Y. Ye and S. Knights, *J Power Sources*, 2013, **238**, 144-149.
24. A. Masao, S. Noda, F. Takasaki, K. Ito and K. Sasaki, *Electrochemical and Solid-State Letters*, 2009, **12**, B119-B122.
25. P. Zhang, S.-Y. Huang and B. N. Popov, *J Electrochem Soc*, 2010, **157**, B1163-B1172.
26. J. Parrondo, F. Mijangos and B. Rambabu, *J Power Sources*, 2010, **195**, 3977-3983.
27. M. Dou, M. Hou, D. Liang, W. Lu, Z. Shao and B. Yi, *Electrochim Acta*, 2013, **92**, 468-473.
28. M. Batzill and U. Diebold, *Progress in Surface Science*, 2005, **79**, 47-154.
29. M. Yin, J. Y. Xu, Q. F. Li, J. O. Jensen, Y. J. Huang, L. N. Cleemann, N. J. Bjerrum and W. Xing, *Appl Catal B-Environ*, 2014, **144**, 112-120.
30. K. Sasaki, F. Takasaki, Z. Noda, S. Hayashi, Y. Shiratori and K. Ito, *Ecs Transactions*, 2010, **33**, 473-482.
31. S. Oswald, G. Behr, D. Dobler, J. Werner, K. Wetzig and W. Arabczyk, *Anal Bioanal Chem*, 2004, **378**, 411-415.

32. D. Dobler, S. Oswald, J. Werner, W. Arabczyk, G. Behr and K. Wetzig, *Chem Phys*, 2003, **286**, 375-383.
33. V. Dusastre and D. E. Williams, *J Phys Chem B*, 1998, **102**, 6732-6737.
34. D. G. Stroppa, L. A. Montoro, A. Beltran, T. G. Conti, R. O. da Silva, J. Andres, E. R. Leite and A. J. Ramirez, *Chem-Eur J*, 2011, **17**, 11515-11519.
35. Y. M. Cross and D. R. Pyke, *J Catal*, 1979, **58**, 61-67.
36. D. Szczuko, J. Werner, G. Behr, S. Oswald and K. Wetzig, *Surf Interface Anal*, 2001, **31**, 484-491.
37. D. Szczuko, J. Werner, S. Oswald, G. Behr and K. Wetzig, *Appl Surf Sci*, 2001, **179**, 301-306.
38. Wakabaya.K, Y. Kamiya and N. Ohta, *B Chem Soc Jpn*, 1967, **40**, 2172-&.
39. T. J. Schmidt, H. A. Gasteiger, G. D. Stab, P. M. Urban, D. M. Kolb and R. J. Behm, *J Electrochem Soc*, 1998, **145**, 2354-2358.
40. B. Schwanitz, A. Rabis, M. Horisberger, G. G. Scherer and T. J. Schmidt, *Chimia*, 2012, **66**, 110-119.
41. A. Ohma, K. Shinohara, A. Iiyama, T. Yoshida and A. Daimaru, *ECS Transaction*, 2011, **41**, 775-784.
42. U. A. Paulus, T. J. Schmidt, H. A. Gasteiger and R. J. Behm, *J Electroanal Chem*, 2001, **495**, 134-145.
43. H. V. Fajardo, E. Longo, L. F. D. Probst, A. Valentini, N. L. V. Carreno, M. R. Nunes, A. P. Maciel and E. R. Leite, *Nanoscale Res Lett*, 2008, **3**, 194-199.
44. C. Terrier, J. P. Chatelon, R. Berjoan and J. A. Roger, *Thin Solid Films*, 1995, **263**, 37-41.
45. B. Slater, C. R. A. Catlow, D. H. Gay, D. E. Williams and V. Dusastre, *J Phys Chem B*, 1999, **103**, 10644-10650.
46. C. S. Rastomjee, R. G. Egdell, M. J. Lee and T. J. Tate, *Surf Sci*, 1991, **259**, L769-L773.
47. J. T. S. Irvine, D. C. Sinclair and A. R. West, *Adv Mater*, 1990, **3**, 132-138.
48. J. Sanchez-Gonzalez, A. Macias-Garcia, M. F. Alexandre-Franco and V. Gomez-Serrano, *Carbon*, 2005, **43**, 741-747.
49. W. H. Haynes, *CRC Handbook of Chemistry and Physics, 94th Edition*, 2013, CRC Press Boca Raton.
50. B. Schwanitz, H. Schulenburg, M. Horisberger, A. Wokaun and G. G. Scherer, *Electrocatalysis-Us*, 2011, **2**, 35-41.
51. K. J. J. Mayrhofer, B. B. Blizanac, M. Arenz, V. R. Stamenkovic, P. N. Ross and N. M. Markovic, *J Phys Chem B*, 2005, **109**, 14433-14440.
52. E. Fabbri, S. Taylor, A. Rabis, P. Levecque, O. Conrad, R. Kötz and T. J. Schmidt, *Chemcatchem*, 2014, **DOI: 10.1002/cctc.201300987**.
53. N. M. Markovic, H. A. Gasteiger and P. N. Ross, *J Phys Chem-Us*, 1995, **99**, 3411-3415.
54. K. J. J. Mayrhofer, J. C. Meier, S. J. Ashton, G. K. H. Wiberg, F. Kraus, M. Hanzlik and M. Arenz, *Electrochem Commun*, 2008, **10**, 1144-1147.
55. M. Peuckert, T. Yoneda, R. A. D. Betta and M. Boudart, *J Electrochem Soc*, 1986, **133**, 944-947.
56. A. Gamez, D. Richard, P. Gallezot, F. Gloaguen, R. Faure and R. Durand, *Electrochim Acta*, 1996, **41**, 307-314.
57. O. V. Cherstiouk, P. A. Simonov and E. R. Savinova, *Electrochim Acta*, 2003, **48**, 3851-3860.
58. F. Maillard, S. Schreier, M. Hanzlik, E. R. Savinova, S. Weinkauf and U. Stimming, *Phys Chem Chem Phys*, 2005, **7**, 385-393.
59. S. Kunz, K. Hartl, M. Nesselberger, F. F. Schweinberger, G. Kwon, M. Hanzlik, K. J. J. Mayrhofer, U. Heiz and M. Arenz, *Phys Chem Chem Phys*, 2010, **12**, 10288-10291.
60. M. Nesselberger, M. Roefzaad, R. Fayçal Hamou, P. Ulrich Biedermann, F. F. Schweinberger, S. Kunz, K. Schloegl, G. K. H. Wiberg, S. Ashton, U. Heiz, K. J. J. Mayrhofer and M. Arenz, *Nat Mater*, 2013, **12**, 919-924.
61. K. J. J. Mayrhofer, B. B. Blizanac, M. Arenz, V. R. Stamenkovic, P. N. Ross and N. M. Markovic, *The Journal of Physical Chemistry B*, 2005, **109**, 14433-14440.
62. A. Lewera, L. Timperman, A. Roguska and N. Alonso-Vante, *J Phys Chem C*, 2011, **115**, 20153-20159.